PCCP

Theoretical H + O3 rate coefficients from ring polymer molecular dynamics on an accurate global potential energy surface: Assessing experimental uncertainties

Journal:	*Physical Chemistry Chemical Physics*
Manuscript ID	CP-ART-11-2020-005771.R1
Article Type:	Paper
Date Submitted by the Author:	16-Dec-2020

Complete List of Authors:	Chen, Qixin; Nanjing University, School of Chemistry and Chemical Engineering Hu, Xixi; Nanjing University, Kuang Yaming Honors School Guo, Hua; University of New Mexico, Department of Chemistry and Chemical Biology Xie, Daiqian; Nanjing University, School of Chemistry and Chemical Engineering

Submitted to *Phys. Chem. Chem. Phys.*, November 5, 2020, revised on December 16, 2020

Theoretical H + O_3 rate coefficients from ring polymer molecular dynamics on an accurate global potential energy surface: Assessing experimental uncertainties

Qixin Chen,[a] Xixi Hu,[b,*] Hua Guo,[c] and Daiqian Xie[a]

[a] *Institute of Theoretical and Computational Chemistry, Key Laboratory of Mesoscopic Chemistry, School of Chemistry and Chemical Engineering, Nanjing University, Nanjing 210093, China*

[b] *Kuang Yaming Honors School, Nanjing University, Nanjing 210023, China*

[c] *Department of Chemistry and Chemical Biology, University of New Mexico, Albuquerque, New Mexico 87131, USA*

*: Corresponding author, xxhu@nju.edu.cn

Abstract

Thermal rate coefficients and kinetic isotope effects have been calculated for an important atmospheric reaction H/D + O_3 → OH/OD + O_2 based on an accurate permutation invariant polynomial-neural network potential energy surface, using ring polymer molecular dynamics (RPMD), quasi-classical trajectory (QCT) and variational transition-state theory (VTST) with multidimensional tunneling. The RPMD approach yielded results that are in generally better agreement with experimental rate coefficients than the VTST and QCT ones, especially at low temperatures, attributable to its capacity to capture quantum effects such as tunneling and zero-point energy. The theoretical results support one group of existing experiments over the other. In addition, rate coefficients for the D + O_3 → OD + O_2 are also reported using the same methods, which will allow a stringent assessment of future experimental measurements, thus helping to reduce the uncertainty in the recommended rate coefficients of this reaction.

1 Introduction

Hydrogen atom is one of two atomic species critical to the photochemistry and energy balance in the Earth's mesopause region between approximately 80 and 100 km in altitude. As the mainly loss mechanism, atomic hydrogen participates in the highly exothermic reaction $H(^2S) + O_3(X^1A_1) \rightarrow OH(X^2\Pi) + O_2(X^3\Sigma_g^-)$ to produce vibrationally excited hydroxyl radicals up to $\upsilon = 9$, which is known to be responsible for Meinel overtone bands of the hydroxyl radical in the airglow.[1] Because of the lack of transitions in the visible and infrared regions, the H atom concentration in the mesopause is difficult to measure directly. However, it can be derived from the large data set of mesospheric Meinel emission observations from the SABER instrument[2] and ozone concentrations determined from its infrared emissions.[3] Indeed, the H atom concentration is proportional to the rate coefficients for the H + O_3 reaction.[3] Consequently, accurate and reliable rate coefficients for the title reaction, particularly at the temperature of mesopause, are highly desirable.

In the past several decades, many experiments have been performed to measure the rate coefficient of the title reaction. However, kinetic measurements involving radicals are often plagued with large uncertainties. Phillips and Schiff carried out in 1962 an experiment to measure the rate coefficients using discharge flow mass spectrometry.[4] Because the experiment involved high H and O_3 concentrations and used short reaction times which causes incomplete mixing and non-isothermal conditions, their value at 298 K is now considered unreliable.[5] Later, Clyne and Monkhouse performed discharge flow resonance fluorescence measurements from 298 to 638 K.[5]

A similar experiment by Keyser[6] extended the range of measurement down to 196 K, but their values differed significantly from those of Clyne and Monkhouse,[5] but agreed with VUV flash photolysis resonance lamp measurement down to 219 K by Lee *et al*.[7] In 1982, Greenblatt and Wiesenfeld[8] reported their value at 298 K, 1.5×10^{-11} cm^3/s, which is very close to the value of Clyne and Monkhouse, $(1.76\pm0.21)\times10^{-11}$ cm^3/s. The latest experiment was performed by Liu *et al*. employing time-resolved laser photolysis-laser-induced fluorescence.[9] It should be noted that their results for the first time covered the range of 150-180 K, relevant to those in the mesopause region. To summarize, the room temperature results can be divided into two groups. Clyne and Monkhouse, and Greenblatt and Wiesenfeld, are referred to as Group I. The other three sets of values, which are about twice as large as the values in Group I, are referred to as Group II. The latter have been used as the basis for the recommended rate coefficients of the title reaction.[10, 11] The measurement of Liu *et al*. is the only data covering lower temperatures which is important to atmospheric chemistry. From the experimental perspective, much uncertainty still remains, due presumably to experimental complications such as secondary reactions. Hence, it is highly desirable to provide an independent assessment of the experimental data from accurate theoretical approaches.

Theoretically, many *ab initio* calculations have been reported, and much progress has been made towards a better understanding of the kinetics and dynamics of the H + O_3 reaction, which leads exoergically to both the OH + O_2 and HO_2 + O channels. In this work, we will focus on the former, as the latter product channel is known to be negligible for the title reaction in the temperature range studied by this work.[12, 13]

However, we note in passing there have been many studies focused on kinetics and dynamics of the related $O + HO_2 \rightarrow OH + O_2$ reaction[14-20] and properties of the HO_3 radical.[21-34] In a pioneering study in 1997, Varandas and Yu employed the double many-body expansion (DMBE) method to construct the first global PES for the ground state HO_3 (DMBE I PES) at the unrestricted configuration interaction with single and double electron excitations (UCISD) level of theory with the 6-311G++(d, p) basis set.[21] This DMBE I PES predicted a shallow van der Waals (vdW) minimum and a submerged barrier in the $H + O_3$ entrance channel, a significant energy barrier for the dissociation of HO_3 to $OH + O_2$, and a metastable HO_3 well with an out-of-plane structure. The dissociation barrier and the out-of-plane HO_3 structure are now known to be inconsistent with experimental observations[35, 36] and more accurate *ab initio* calculations.[30, 34, 37, 38] Based on this PES, quasi-classical trajectory (QCT),[39] reduced-dimensional quantum dynamics with three coordinates (3D-QD),[40, 41] and variational transition-state theory (VTST)[17] were used to calculate the thermal rate coefficient. The QCT results showed good agreement with the experimental rate coefficients of Lee *et al*. and Keyser *et al*. at high temperatures.[42-45] Meanwhile, due to the reduced-dimensional nature, 3D-QD[40, 41] gave much smaller rate coefficients than all the experimental values, thus not reliable. Besides, the results from both microcanonical unified statistical theory and microcanonical VTST[17] are significantly larger than all experimental values, presumably due to the absence of an entrance channel barrier. Four years later, an improved DMBE II PES was constructed by adding 5038 QCISD(T)/CBS points to the HO_3 complex region and the $OH + O_2$ asymptotic region

to improve the description of the two stable HO_3 isomers.[22] Because PES in the H + O_3 channel was barely changed, the DMBE II PES is not expected to change the rate coefficient of the title reaction. Overall, the theoretically calculated rate coefficients in the literature may not be reliable due to the uncertainties of the PES, particularly in the entrance channel.

To improve our understanding of the kinetics and dynamics of the title reaction, we have recently constructed an accurate global PES for the ground electronic state of HO_3. The PES was based on 21452 points calculated using an explicitly correlated version of the multi-reference configuration interaction method with the Davidson correction (MRCI-F12+Q) with a double zeta basis set designed for the F12 approach (VDZ-F12).[20] As discussed in our previous publication,[20] the use of the MRCI method is vital in dealing with the multi-reference nature of the system. These *ab initio* points were represented by the high-fidelity permutation invariant polynomial-neural network (PIP-NN) approach with a root mean square fitting error of 0.20 kcal/mol. As shown in Fig. 1, a key feature that differs from the DMBE PESs is the presence of a small barrier in the entrance channel, which is expected to reduce the rate coefficients reported in previous theoretical studies.[17] Although full-dimensional quantum treatments of the reaction dynamics would be ideal to extract the rate coefficients, such calculations involving three heavy oxygen atoms are still very difficult, if not impossible.[46] On the other hand, transition-state theory (TST) offers a much more efficient theoretical approach for calculating rate coefficients, but the proper inclusion of the multidimensional tunneling is essential. To this end, many semi-classical models have

been proposed,[47, 48] but the reliability of these approximations is still uncertain, especially in the deep tunneling regime. In the past decade, a new approximate quantum rate theory based on ring polymer molecular dynamics (RPMD)[49-53] has been developed and successfully applied to a wide variety of reactions.[53-90] This method is based on an isomorphism between statistic properties of a quantum system and a classical ring polymer,[91] and has a clear relationship with the quantum mechanical version of TST. It is able to capture quantum effects such as ZPE and tunneling within the same framework. Indeed, comparisons with quantum mechanically obtained rate coefficients of benchmark systems have been quite impressive.[92] Since classical trajectories are used, furthermore, the scaling of RPMD calculation is quite favorable with respect to the number of atoms.

In this work, we report a theoretical study of the kinetics of the title reaction and its deuterated counterpart using three different approaches: RPMD, QCT, and VTST with multidimensional tunneling, using the recently published PIP-NN PES.[20] Through these calculations, we hope to assess the accuracy of the PES and the importance of quantum effects, particularly at low temperatures. Comparisons with the existing experimental results may also shed light on the reliability and self-consistency of these data. The paper is organized as follows. Section II outlines the details of RPMD, QCT, and VTST calculations. The results and discussion are present in Section III. Finally, conclusions are given in Section IV.

2 Methods

2.1 Ring polymer molecular dynamics calculations

The RPMD method exploits the isomorphism between the statistical properties of a quantum system and those of a fictitious classical ring polymer made up of harmonically connected beads.[58, 91, 93] There are several desirable features in the RPMD approach to the reaction rate.[49-51] For instance, the RPMD theory recovers the classical TST at high temperatures. In the limit of no recrossing, the RPMD rate is equivalent to the quantum TST, which serves as an upper bound.[94, 95] The dynamical recrossing, which is strongly influenced by tunneling, is approximately included in the RPMD rate theory as a transmission coefficient. Furthermore, the RPMD result do not depend on the choice of the dividing surface, which can be quite difficult to define for high-dimensional systems. In addition, there is a clear connection to semiclassical instanton theory, which makes RPMD reasonably reliable in the deep tunneling regime.[94] The RPMD method has been validated by comparing with exact quantum rate calculations for prototypical systems.[92] As classical trajectories are used to compute the relevant properties, it is also numerically efficient and scales well with the size of the system.

It is convenient to express the RPMD rate coefficient at temperature T in the following form via the Bennett-Chandler factorization:[52, 96-98]

$$k_{\mathrm{RPMD}}(T) = g_{\mathrm{e}}(T)\, k_{\text{cd-QTST}}\left(T;\xi^{\ddagger}\right)\kappa\left(t\to+\infty;\xi^{\ddagger}\right). \quad (1)$$

where ξ is the reaction coordinate. The $g_{\mathrm{e}}(T)$ is the electronic degeneracy, namely the ratio of the electronic partition functions. For the H + O_3 reaction, the electronic degeneracy is two for the doublet atomic hydrogen, one for the singlet ozone molecule in its ground electronic state, and two for the transition state because it is on a doublet

state of HO_3. Therefore, the electronic degeneracy for the H + O_3 reaction is equal to one.

The second term $k_{\text{cd-QTST}}\left(T;\xi^{\ddagger}\right)$ denotes the static contribution to the rate coefficient, which comes from the centroid-density quantum TST,[99, 100] and is evaluated from the free-energy difference ($W\left(\xi^{\ddagger}\right)-W\left(0\right)$) between the reactant channel and the top of the centroid potential of mean force (PMF),[52, 53, 98] $\xi^{\ddagger}$:

$$k_{\text{cd-QTST}}\left(T;\xi^{\ddagger}\right)=4\pi R_{\infty}^{2}\left(\frac{m_A+m_B}{2\pi\beta m_A m_B}\right)^{1/2} e^{-\beta\left[W\left(\xi^{\ddagger}\right)-W(0)\right]}, \tag{2}$$

where $4\pi R_{\infty}^{2}\left(\left(m_A+m_B\right)/2\pi\beta m_A m_B\right)^{1/2}$ is the surface area of a sphere of radius R_{∞} times the thermally averaged speed of the reactants (A and B) entering this sphere and $\beta=(k_B T)^{-1}$ with k_B as the Boltzmann constant.

Finally, $\kappa\left(t\to+\infty;\xi^{\ddagger}\right)$ is the dynamical correction, which can be expressed as a ratio of ring polymer flux-side correlation function ($c_{fs}^{(n)}$) at the dividing surface in two different time limits:[52, 53]

$$\kappa\left(t\to+\infty;\xi^{\ddagger}\right)=\frac{c_{fs}^{(n)}\left(t\to+\infty;\xi^{\ddagger}\right)}{c_{fs}^{(n)}\left(t\to 0^{+};\xi^{\ddagger}\right)}. \tag{3}$$

The interplay between the static $k_{\text{cd-QTST}}\left(T;\xi^{\ddagger}\right)$ and dynamic $\kappa\left(t\to+\infty;\xi^{\ddagger}\right)$ terms ensures that the RPMD rate coefficient is independent of the choice of the dividing surface.[52, 53, 61, 98]

The minimal number of beads needed to converge the RPMD calculations can be estimated by the following formula:[101]

$$n_{\min}=\beta\hbar\omega_{\max}, \tag{4}$$

where $\omega_{\max}$ is the largest frequency of the system, which is 729.13 cm^{-1} for the H +

O_3 reaction and 536.04 cm^{-1} for the D + O_3 reaction.[20] There is another important parameter, namely crossover temperature: $T_c = \hbar\omega_{TS}/2\pi k_B$, which is used to characterize the importance of quantum tunneling. The temperature range below T_c is often referred as to the deep tunneling regime. In addition, the RPMD rate regresses back into the classical limit when only one bead is used.[52] This quantity offers a clear measure on the influence of the quantum effects, namely ZPE and tunneling.

All RPMD rate calculations in this work were performed using RPMDrate[98] developed by Suleimanov. In the calculation of the PMF using the umbrella integral method,[102, 103] three different window sizes have been used to handle different regions along the reaction coordinate. In the relatively flat asymptotic region ($\xi \in [-0.03, 0.66]$), windows with an equal size ($\Delta\xi = 0.03$) were used with the force constant of the biasing potential of $k = 0.068(T/\mathrm{K})$ eV . In the region before the barrier ($\xi \in [0.67, 0.90]$), the force constant of the biasing potential increases to $2.721(T/\mathrm{K})$ eV , with the window size decreasing to 0.01 accordingly. To ensure accurate sampling near the barrier ($\xi \in [0.67, 0.90]$), larger *k* values ($8.163\sim13.605(T/\mathrm{K})$ eV) were used with the width of windows reduced to 0.005. In each umbrella sampling window, the system was first equilibrated for 20 ps, then the sampling was performed for 6 ns in the NVT (constant volume and temperature) ensemble. The final PMF was obtained by splicing the segments together. All simulations were under the Andersen thermostat.[104] To calculate the transmission coefficient, the initial positions of the trajectories for computing the flux-side correlation functions were saved from the configurations of a parent trajectory with the

centroid of ring polymer restricted at the top of the PMF curve via the SHAKE algorithm.[105] For each initial configuration, sampled once every 2 ps, 100 separate NVE child trajectories were propagated without constraint for 100 fs to make sure the transmission coefficient reaches its plateau value. The time step is 0.1 fs for all the RPMD calculations. The calculation parameters are summarized in the Table 1.

2.2 QCT calculations

In this work, the QCT methodology for both the H + O_3 and D + O_3 reactions is similar to the ones in our recent work.[20] All the calculations were carried out using the VENUS program package.[106, 107] To calculate the thermal reaction rate at selected temperatures, batches of 120000 trajectories starting from the H + O_3 channel were run on the PIP-NN PES. The maximal impact parameter b_{max} was determined to be 3.0 Å for both the H + O_3 and D + O_3 reactions over the entire temperature range of 150-640 K after the test of a small set of trajectories. The sampling of the initial relative translational energy and ro-vibrational energies of reactants were performed from the Boltzmann distribution at each temperature. The time step in the integral of motion was selected to be 0.1 fs to converge the energy of most trajectories within 0.01 kcal/mol.

Accordingly, the rate coefficient can be calculated by the Monte Carlo expression

$$k(T) = g_e(T)\left(\frac{8k_B T}{\pi\mu}\right)^{1/2} \pi b_{max}{}^2 \frac{N_r}{N_{tot}}, \quad (5)$$

in which N_r and N_{tot} are the numbers of reactive and total trajectories. μ is the reduced mass of the reactants. As discussed above, the electronic degeneracy factor (g_e) is chosen to be 1 for the H + O_3 reaction. The statistical error is given by

$\sigma_{\mathrm{r}} = \left[\left(N_{\mathrm{tot}} - N_{\mathrm{r}} \right) / \left(N_{\mathrm{tot}} N_{\mathrm{r}} \right) \right]^{1/2}$.

We note that the QCT results reported in Ref. 20 used a hard correction scheme for ZPE violation, in which both the reactive and non-reactive trajectories were subjected to such a correction. In such a way, many trajectories in the non-reactive channel were eliminated. By comparing those QCT results with corresponding RPMD ones, it becomes clear that this hard ZPE correction scheme led to inflated rate coefficients for the reaction. In order to make a meaningful comparison with the classical limit of the RPMD calculations, we did not impose any restrictions on the ZPE violating trajectories in this work.[20] This is reasonable as the rate is largely determined by the entrance channel barrier and the ZPE violating trajectories have a very small chance to exit from the reactant channel because of the large exothermicity of the reaction.

2.3 Variational transition-state theory calculations

All VTST rate calculations have been obtained using the Polyrate program.[108] The rate coefficient in canonical VTST[47, 109] can be calculated by the following expression:

$$k^{\mathrm{CVT}/\mu\mathrm{OMT}}(T) = \kappa^{\mathrm{tun}}(T) \cdot k^{\mathrm{CVT}}(T) . \quad (6)$$

The first term $\kappa^{\mathrm{tun}}(T)$ is the tunneling transmission coefficient calculated using the microcanonical optimized multidimensional tunneling (μOMT) method.[110] In this method, the small-curvature (SCT) and large-curvature (LCT) tunneling probabilities were both calculated, then the larger one is chosen to be the better estimation. The canonical variational TST (CVT) rate $k^{\mathrm{CVT}}(T)$ was calculated by the following formula:

$$k^{\mathrm{CVT}}(T) = g_{\mathrm{e}}(T)\sigma_{\mathrm{sym}}\frac{k_{\mathrm{B}}T}{h}K^{\circ}\min_{s}\exp\left[\frac{-\Delta G^{\mathrm{GT},\circ}(T,s)}{k_{\mathrm{B}}T}\right], \quad (7)$$

where σ_{sym} is the symmetry factor or number of equivalent paths, K° is the reciprocal of the standard state concentration, $1\,\mathrm{molecule}\cdot\mathrm{cm}^3$. To estimate $\Delta G^{\mathrm{GT},\circ}(T,s)$, the vibrational partition functions were calculated as quantum harmonic oscillators,[111-113] while the rotational partition functions were calculated classically. The dividing surface was varied at each temperature to ensure the maximum of the free-energy of activation. Because of two equivalent approaches of H towards ozone, the symmetry number for the reaction is 2.

3 Results and discussion

3.1 Properties of the minimum energy path

In this work, we utilized the PIP-NN PES of the ground state HO_3 to carry out the kinetics calculations for the H + O_3 and D + O_3 reactions. The construction of this PES has been described in detail in our previous work,[20] so we only outline the landscape of the reaction channel here. As shown in Fig. 1, PIP-NN PESs have a vdW well in the entrance channel, which is similar to that found in the DMBE I PES. Different from the DMBE I PES,[21] in which the entrance channel saddle point lies 0.48 kcal/mol below reactant asymptote, the PIP-NN PES has a small barrier that lies 0.86 kcal/mol above the reactant asymptote.[20] In Fig. 2a, the aforementioned features are all visible in the entrance and exit channels of the PES contour plot for the H + O_3 → OH + O_2 reaction, in which the barrier and vdW well are marked by a square and a circle, respectively. In Fig. 2b, the minimum energy path (MEP) and vibrationally adiabatic

ground-state potential energy (V_a^G) calculated using Polyrate are shown as for the H + O_3 → OH + O_2 reaction as a function of the mass-dependent intrinsic reaction coordinate (IRC) *s*. The MEP shows an asymmetrical profile because the reaction is highly exothermic.

3.2 RPMD rate coefficients

Figure 3 collects the converged RPMD PMF curves for both the H/D + O_3 reactions at different temperatures in the left panels and corresponding transmission coefficients in the right panels. At all temperatures, the PMFs for both reactions have a peak near $\xi = 1$, due apparently to the small potential barrier in the entrance channel. There is a strong temperature dependence in the PMF barrier height, underscoring the increasing importance of tunneling at low temperatures, which lowers the effective barrier. The signature of tunneling also emerges as an isotope effect in the PMF. Although the free-energy barrier at high temperature is about the same for the two isotopologues, the free-energy barrier of the D + O_3 reaction at low temperature is significantly higher than that of the H + O_3 reaction. Since the reaction coordinate is based on the ring polymer centroid, the internal modes of the ring polymer begin to contribute to the optimum reaction coordinate for an asymmetric reaction as soon as the temperature passes below crossover temperature.[54, 94] As a result, the reaction coordinate of the PMF barrier ($\xi^{\ddagger}$) is somewhat shifted away from 1 at 150 K.

Quantum effects also manifest in the transmission coefficients. From 298 K to 640 K, there is no significant difference in the RPMD transmission coefficients between the

reactions. Their values close to unity indicate that recrossing has only a minor impact on the rate coefficients. However, the transmission coefficient begins to decrease dramatically from 220 K and 150 K for the H + O_3 and D + O_3 reactions, respectively, signaling strong recrossing. The small transmission coefficients are suggestive of increasing impact of tunneling, which is more drastic for the lighter isotope. We note in passing that all RPMD trajectories eventually reach the HO + O_2 product channel and there was no trajectory found in the HO_2 + O channel, confirming the experimental finding that the latter channel is negligible.[12, 13]

To further illustrate the importance of quantum effects, we show in Fig. 4 the calculated PMFs along the reaction coordinate and the time-dependent transmission coefficients for 1-bead and the converged number of beads at 150 K and 640 K for both H + O_3 and D + O_3 reactions. At a given temperature, their classical free-energy barriers have almost the same position and height, as the two reactions are identical in the classical limit. When quantum effects are included in the converged RPMD, the corresponding free-energy barriers are systematically lower than the classical ones, although the differences are small at 640 K. At the lower temperature (150 K), the difference is large for the H + O_3 reaction because tunneling is more facile than the D + O_3 reaction. It is interesting to note that the crossover temperature is 166.96 K for the H + O_3 reaction and 122.75 K for the deuterated reaction, below which tunneling plays an important role. This is consistent with the results.

As discussed above, recrossing in this system is significant, particularly at low temperatures. This is presumably due to two factors. The first is the relatively loose

transition state of the reaction, while the second is tunneling. Indeed, large differences are seen in the RPMD transmission coefficients with different numbers of beads, particularly at low temperature where tunneling dominates. As expected, the recrossing behavior is similar at 640 K for both reactions, but the divergence is quite large at 150 K. Indeed, the transmission coefficient of the H + O_3 reaction at 150 K is only 0.082, almost one-sixth of that for the deuterated reaction at 150 K. To further estimate the tunneling effect, the classical limit transmission coefficient at 150 K is calculated, which located at the same reaction coordinate, $\xi = 0.941$, as the converged one. To some degree, the difference can reflect the importance of tunneling. Comparing with the quantum case, the classical value (0.011) is quite small, which indicates the leading role of tunneling at low temperature. This behavior is quite different from the Cl + O_3 reaction, where transmission coefficients are almost the same for 1-bead and the converged number of beads at 200 K and 400 K,[57] because tunneling is not important.

3.3 Comparison with experiments and other theories

The calculated RPMD rate coefficients are summarized in Tables 2 and 3 for the H + O_3 and D + O_3 reactions, respectively. The rate coefficients of CVT/μOMT and QCT are also listed in two tables for comparison. As shown in Fig. 5, the RPMD thermal rate coefficients for H + O_3 reaction gradually decrease with decreasing temperature, which is apparently a consequence of the potential barrier. This is consistent with the general experimental trend. It is clear that the RPMD rate coefficients deviate significantly from the Arrhenius relation at low temperatures, due

to tunneling. Many previous studies have shown that RPMD generally overestimates the rate coefficients of a reaction with an asymmetric barrier in the deep tunneling regime.[92] But 150 K is very close to the crossover temperature 167 K in our case, so the systematic error is probably quite small. It is worth mentioning that the differences between the current QCT values and those reported in our previous work[20] stem from the "hard" ZPE correction scheme for the non-reactive trajectories in the latter, which led to the overestimation the number of invalid trajectories for non-reactive case.

Over the temperature range from 298 to 640 K, the RPMD rate coefficient is in good agreement with the Group I of experimental values of Clyne and Monkhouse[5] and Greenblatt and Wiesenfeld,[8] but only about half of the other experimental values (Group II). At 150 K, the RPMD result lies in the range of the experimental value of Liu *et al*.[9] It is interesting that the rate coefficient reported by these authors from 220 K to 300 K fall within the Group II of experimental data, which are much larger than the theory. The sources of the experimental uncertainties are unknown, but most likely due to secondary regeneration of H atoms. For this reason, these authors corrected the rate constants by running the kinetic model based on the NASA-JPL[11] rate coefficients under the same experimental conditions.[9] This casts some doubt on the validity of their data and suggests the need for further investigations on the origin of the inconsistency in the experimental rate data.

As shown in Fig. 5, the NASA-JPL recommended rate coefficient for the title reaction is given in the Arrhenius form for the high temperature range, which clearly indicates an activated process. If these data were indeed accurate, one would expect

higher rates than those reported by Liu *et al*. at lower temperatures, due to tunneling over the barrier, as shown in theory. However, this is obviously not the case, as shown in Fig. 5, in which the low-temperature experimental data are on the NASA line. This observation suggests that the Group II experimental data may be overestimated in the high temperature range. On the other hand, the high-temperature experimental values of Clyne and Monkhouse[5] and Greenblatt and Wiesenfeld[8] and the low temperature data of Liu *et al*.[9] deviate from the Arrhenius line, in excellent agreement with our theoretical predictions, suggesting the Group I experimental measurements at high temperature are more consistent with the low-temperature data.

An independent validation of the aforementioned conclusion is to examine the kinetics of the deuterated isotopolog of the title reaction. The RPMD, CVT/μOMT, QCT rate coefficients for the deuterated reaction are presented in Fig. 6. The behaviors of these results are similar to those discussed above, although the differences become smaller, due to smaller quantum effects. Unfortunately, there has so far been no experimental study on this reaction.

It is also clear from Fig. 5 that the QCT are much smaller than the RPMD rate coefficient at low temperatures due to its complete neglect of tunneling, but their agreement improves at high temperatures, as expected. The CVT/μOMT results also smaller than the RPMD rate coefficient, although the underestimation at low temperatures is much less, due apparently to the approximate inclusion of tunneling. Similar behaviors can be seen in Fig. 6 for the deuterated counterpart.

Comparing with previous theoretical results, the RPMD rate coefficients on the new

PES are in much better agreement with the experimental values than the μVT values of Fernández-Ramos and Varandas[17], the 3D-QD values of Szichman *et al.*[40, 41] and the QCT results of Yu and Varandas.[39] based on the DMBE I PES. The major errors of these previous theoretical results are likely due to the inaccuracies in the PES, particularly in the reactant channel.

3.4 Kinetic isotope effects

Kinetic isotope effects (KIEs) provide useful information on the mechanisms for many chemical processes, which can be obtained using both experimental and theoretical means.[114] The KIE can sometimes help to resolve inconsistencies in the experimental data, as shown in our recent kinetic study on the OH + HCl reaction.[72] This is because it mitigates the systematic errors in the rate coefficients.

The primary KIE for the title reaction is shown in Fig. 7 for the H and D isotopomers. It is interesting that the QCT KIEs based on DMBE I PES almost the same as the QCT KIEs and the classical limit KIEs based on the PIP-NN PES. In contrast to the QCT KIE, the KIE from the RPMD and CVT/μOMT calculations gradually increase with the decreasing temperature, due apparently to the quantum effects dominant at low temperatures. The differences between RPMD and CVT/μOMT stem presumably from harmonic approximation for the vibrational partition function in the CVT calculations and the approximate characterization of tunneling in the μOMT approximation. The rate coefficients of the deuterated reaction and KIE can be used in the future comparison with experimental data to further assess the accuracy of the PES.

4 Conclusions

The kinetics of the H + O_3 reaction and its deuterated counterpart have been investigated theoretically in this work on a recently developed accurate PIP-NN PES. Several theoretical methods, namely RPMD, QCT and VTST, were used to compute the thermal rate coefficients. The agreement between the RPMD results and experimental values for the H + O_3 reaction is significantly improved compared with previous theoretical calculations, thanks to a higher quality PES and the inclusion of quantum effects. The non-Arrhenius behavior at low temperatures is observed in the RPMD rate coefficients due to tunneling. These quantum effects also manifest a primary KIE, which plays a more important role in the H + O_3 reaction while less tunneling occurs in the D + O_3 reaction. The accurate RPMD rate coefficients are used to assess the available experimental data, which are quite scattered and contain large uncertainties. One group of experimental rate coefficients are identified to be more accurate given their good agreement with theory. New experiments, particularly for the D + O_3 reaction at low temperatures, are highly desirable to provide a more reliable comparison between theory and experiment and a more rigorous assessment of the accuracy of the PES. A more accurate kinetic characterization of the title reaction will also help to better understand chemical processes in the atmosphere.

Conflicts of interest

The authors declare no competing financial interest.

Acknowledgements

This work was supported by National Natural Science Foundation of China (grant nos. U1932147 and 22073042 to X.H., 21733006 to D. X.), by the Fundamental Research Funds for the Central Universities (grant no. 14380016 to X.H.), and in part by US Department of Energy (grant no. DE-SC0015997to H.G.). We are grateful to the High Performance Computing Center (HPCC) of Nanjing University for doing the RPMD calculations on its blade cluster system. We thank Yongle Li for some helpful discussions.

References

1. A. B. Meinel, *Astrophys. J.*, 1950, **111**, 555-564.
2. J. Mast, M. G. Mlynczak, L. A. Hunt, B. T. Marshall, C. J. Mertens, J. M. Russell, R. E. Thompson and L. L. Gordley, *Geophys. Res. Lett.*, 2013, **40**, 646-650.
3. M. G. Mlynczak, L. A. Hunt, B. T. Marshall, C. J. Mertens, D. R. Marsh, A. K. Smith, J. M. Russell, D. E. Siskind and L. L. Gordley, *J. Geophys. Res. Atmos*, 2014, **119**, 3516-3526.
4. L. F. Phillips and H. I. Schiff, *J. Chem. Phys.*, 1962, **37**, 1233-1238.
5. M. A. Clyne and P. B. Monkhouse, *J. Chem. Soc., Faraday Trans. 2.*, 1977, **73**, 298-309.
6. L. Keyser, *J. Phys. Chem.*, 1979, **83**, 645-648.
7. J. Lee, J. Michael, W. Payne and L. Stief, *J. Chem. Phys.*, 1978, **69**, 350-354.
8. G. D. Greenblatt and J. R. Wiesenfeld, *J. Geophys. Res. Oceans*, 1982, **87**, 11145-11152.
9. Y. Liu, J. Peng, K. Reppert, S. Callahan and G. P. Smith, *J. Phys. Chem. A*, 2016, **120**, 3855-3860.
10. D. L. Baulch, R. A. Cox, P. J. Crutzen, R. F. Hampson, J. A. Kerr, J. Troe and R. T. Watson, *J. Phys. Chem. Ref. Data*, 1982, **11**, 327-496.
11. Sander, S. P.; Friedl, R. R.; Barker, J. R.; Golden, D. M.; Kurylo, M. J.; Wine, P. H.; Abbatt, J. P. D.; Burkholder, J. B.; Kolb, C. E.; Moortgat, G. K. et al. Chemical Kinetics and Photochemical Data for Use in Stratospheric Modeling, Evaluation Number 17, JPL Publication 10-6; Jet Propulsion Laboratory: Pasadena, CA, 2011.
12. C. J. Howard and B. J. Finlayson-Pitts, *J. Chem. Phys.*, 1980, **72**, 3842-3843.
13. B. J. Finlayson-Pitts, T. E. Kleindienst, M. J. Ezell and D. W. Toohey, *J. Chem. Phys.*, 1981, **74**, 4533-4543.
14. A. J. C. Varandas and H. Szichman, *Chem. Phys. Lett.*, 1998, **295**, 113-121.
15. W. Wang, R. González-Jonte and A. J. C. Varandas, *J. Phys. Chem. A*, 1998, **102**, 6935-6941.
16. O. Setokuchi, M. Sato and S. Matuzawa, *J. Phys. Chem. A*, 2000, **104**, 3204-3210.
17. A. Fernández-Ramos and A. J. C. Varandas, *J. Phys. Chem. A*, 2002, **106**, 4077-4083.
18. D. M. Silveira, P. J. S. B. Caridade and A. J. C. Varandas, *J. Phys. Chem. A*, 2004, **108**, 8721-8730.

19. A. J. C. Varandas, *ChemPhysChem*, 2005, **6**, 453-465.
20. J. Zuo, Q. Chen, X. Hu, H. Guo and D. Xie, *J. Phys. Chem. A*, 2020, **124**, 6427-6437.
21. A. J. C. Varandas and H. G. Yu, *Mol. Phys.*, 1997, **91**, 301-318.
22. H. G. Yu and A. J. C. Varandas, *Chem. Phys. Lett.*, 2001, **334**, 173-178.
23. K. Suma, Y. Sumiyoshi and Y. Endo, *Science*, 2005, **308**, 1885-1886.
24. E. L. Derro, T. D. Sechler, C. Murray and M. I. Lester, *J. Chem. Phys.*, 2008, **128**, 244313.
25. C. Murray, E. L. Derro, T. D. Sechler and M. I. Lester, *Acc. Chem. Res.*, 2009, **42**, 419-427.
26. M. E. Varner, M. E. Harding, J. Vázquez, J. Gauss and J. F. Stanton, *J. Phys. Chem. A*, 2009, **113**, 11238-11241.
27. J. M. Anglada, S. Olivella and A. Solé, *J. Chem. Theory Comput.*, 2010, **6**, 2743-2750.
28. J. M. Beames, M. I. Lester, C. Murray, M. E. Varner and J. F. Stanton, *J. Chem. Phys.*, 2011, **134**, 044304.
29. A. J. C. Varandas, *Phys. Chem. Chem. Phys.*, 2011, **13**, 9796-9811.
30. A. J. C. Varandas, *J. Chem. Theory Comput.*, 2012, **8**, 428-441.
31. E. P. Hoy, C. A. Schwerdtfeger and D. A. Mazziotti, *J. Phys. Chem. A*, 2013, **117**, 1817-1825.
32. K. Suma, Y. Sumiyoshi and Y. Endo, *J. Chem. Phys.*, 2013, **139**, 094301.
33. M. A. Bartlett, A. H. Kazez, H. F. Schaefer and W. D. Allen, *J. Chem. Phys.*, 2019, **151**, 094304.
34. X. Hu, J. Zuo, C. Xie, R. Dawes, H. Guo and D. Xie, *Phys. Chem. Chem. Phys.*, 2019, **21**, 13766-13775.
35. S. D. Le Picard, M. Tizniti, A. Canosa, I. R. Sims and I. W. M. Smith, *Science*, 2010, **328**, 1258-1262.
36. M. Tizniti, S. D. Le Picard, A. Canosa, I. R. Sims and I. W. M. Smith, *Phys. Chem. Chem. Phys.*, 2010, **12**, 12702-12710.
37. A. J. C. Varandas, *Phys. Chem. Chem. Phys.*, 2011, **13**, 15619-15623.
38. Y. Zhou, H. Hu, L. Li, H. Hou and B. Wang, *Comput. Theor. Chem.*, 2013, **1026**, 24-30.
39. H. G. Yu and A. J. C. Varandas, *J. Chem. Soc., Faraday Trans.*, 1997, **93**, 2651-2656.
40. H. Szichman, M. Baer and A. J. C. Varandas, *J. Phys. Chem. A*, 1997, **101**, 8817-8821.
41. H. Szichman, M. Baer and A. J. C. Varandas, *J. Phys. Chem. A*, 1998, **102**, 8909-8912.
42. P. E. Charters, R. G. Macdonald and J. C. Polanyi, *Appl. Opt.*, 1971, **10**, 1747-1754.
43. H. Ohoyama, T. Kasai, Y. Yoshimura, H. Kimura and K. Kuwata, *Chem. Phys. Lett.*, 1985, **118**, 263-266.
44. D. Klenerman and I. W. M. Smith, *J. Chem. Soc., Faraday Trans. 2.*, 1987, **83**, 229-241.
45. J. I. Steinfeld, S. M. Adler-Golden and J. W. Gallagher, *J. Phys. Chem. Ref. Data*, 1987, **16**, 911-951.
46. J. Li, B. Zhao, D. Xie and H. Guo, *J. Phys. Chem. Lett.*, 2020, **11**, 8844-8860.
47. D. G. Truhlar, A. D. Isaacson, B. C. Garrett and M. Baer, *The Theory of Chemical Reactions*, 1985.
48. T. L. Nguyen, J. F. Stanton and J. R. Barker, *Chem. Phys. Lett.*, 2010, **499**, 9-15.
49. I. R. Craig and D. E. Manolopoulos, *J. Chem. Phys.*, 2004, **121**, 3368-3373.
50. I. R. Craig and D. E. Manolopoulos, *J. Chem. Phys.*, 2005, **123**, 34102.
51. I. R. Craig and D. E. Manolopoulos, *J. Chem. Phys.*, 2005, **122**, 84106.
52. R. Collepardo-Guevara, Y. V. Suleimanov and D. E. Manolopoulos, *J. Chem. Phys.*, 2009, **130**, 174713.
53. Y. V. Suleimanov, R. Collepardo-Guevara and D. E. Manolopoulos, *J. Chem. Phys.*, 2011, **134**, 044131.

54. R. Perez de Tudela, F. J. Aoiz, Y. V. Suleimanov and D. E. Manolopoulos, *J. Phys. Chem. Lett.*, 2012, **3**, 493-497.
55. Y. Li, Y. V. Suleimanov, J. Li, W. H. Green and H. Guo, *J. Chem. Phys.*, 2013, **138**, 094307.
56. Y. Li, Y. V. Suleimanov, M. Yang, W. H. Green and H. Guo, *J. Phys. Chem. Lett.*, 2013, **4**, 48-52.
57. R. P. de Tudela, Y. V. Suleimanov, M. Menendez, J. F. Castillo and F. J. Aoiz, *Phys. Chem. Chem. Phys.*, 2014, **16**, 2920-2927.
58. Y. Li, Y. V. Suleimanov, W. H. Green and H. Guo, *J. Phys. Chem. A*, 2014, **118**, 1989-1996.
59. Y. Li, Y. V. Suleimanov and H. Guo, *J. Phys. Chem. Lett.*, 2014, **5**, 700-705.
60. R. Perez de Tudela, Y. V. Suleimanov, J. O. Richardson, V. Saez Rabanos, W. H. Green and F. J. Aoiz, *J. Phys. Chem. Lett.*, 2014, **5**, 4219-4224.
61. Y. V. Suleimanov, W. J. Kong, H. Guo and W. H. Green, *J. Chem. Phys.*, 2014, **141**, 244103.
62. K. M. Hickson, J. C. Loison, H. Guo and Y. V. Suleimanov, *J. Phys. Chem. Lett.*, 2015, **6**, 4194-4199.
63. D. J. Arseneau, D. G. Fleming, Y. Li, J. Li, Y. V. Suleimanov and H. Guo, *J. Phys. Chem. B*, 2016, **120**, 1641-1648.
64. K. M. Hickson and Y. V. Suleimanov, *Phys. Chem. Chem. Phys.*, 2016, **19**, 480-486.
65. Q. Meng, K. M. Hickson, K. Shao, J. C. Loison and D. H. Zhang, *Phys. Chem. Chem. Phys.*, 2016, **18**, 29286-29292.
66. S. Rampino and Y. V. Suleimanov, *J. Phys. Chem. A*, 2016, **120**, 9887-9893.
67. Y. V. Suleimanov and J. Espinosa-Garcia, *J. Phys. Chem. B*, 2016, **120**, 1418-1428.
68. J. Zuo, Y. Li, H. Guo and D. Xie, *J. Phys. Chem. A*, 2016, **120**, 3433-3440.
69. J. F. Castillo and Y. V. Suleimanov, *Phys. Chem. Chem. Phys.*, 2017, **19**, 29170-29176.
70. J. Espinosa-Garcia, C. Rangel and Y. V. Suleimanov, *Phys. Chem. Chem. Phys.*, 2017, **19**, 19341-19351.
71. Q. Meng and J. Chen, *J. Chem. Phys.*, 2017, **146**, 024108.
72. J. Zuo, C. Xie, H. Guo and D. Xie, *J. Phys. Chem. Lett.*, 2017, **8**, 3392-3397.
73. S. Bhowmick, D. Bossion, Y. Scribano and Y. V. Suleimanov, *Phys. Chem. Chem. Phys.*, 2018, **20**, 26752-26763.
74. X. Lu, Q. Meng, X. Wang, B. Fu and D. H. Zhang, *J. Chem. Phys.*, 2018, **149**, 174303.
75. I. S. Novikov, Y. V. Suleimanov and A. V. Shapeev, *Phys. Chem. Chem. Phys.*, 2018, **20**, 29503-29512.
76. D. Nunez-Reyes, K. M. Hickson, P. Larregaray, L. Bonnet, T. Gonzalez-Lezana and Y. V. Suleimanov, *Phys. Chem. Chem. Phys.*, 2018, **20**, 4404-4414.
77. Y. V. Suleimanov, A. Aguado, S. Gomez-Carrasco and O. Roncero, *J. Phys. Chem. Lett.*, 2018, **9**, 2133-2137.
78. P. Del Mazo-Sevillano, A. Aguado, E. Jimenez, Y. V. Suleimanov and O. Roncero, *J. Phys. Chem. Lett.*, 2019, **10**, 1900-1907.
79. T. Gonzalez-Lezana, D. Bossion, Y. Scribano, S. Bhowmick and Y. V. Suleimanov, *J. Phys. Chem. A*, 2019, **123**, 10480-10489.
80. J. Li, *Chin. J. Chem. Phys.*, 2019, **32**, 313-318.
81. Q. Liu, L. Zhang, Y. Li and B. Jiang, *J. Phys. Chem. Lett.*, 2019, **10**, 7475-7481.
82. Y. Liu and J. Li, *Phys. Chem. Chem. Phys.*, 2019, **22**, 344-353.
83. X. Lu, X. Wang, B. Fu and D. Zhang, *J. Phys. Chem. A*, 2019, **123**, 3969-3976.
84. M. Menendez, P. G. Jambrina, A. Zanchet, E. Verdasco, Y. V. Suleimanov and F. J. Aoiz, *J. Phys.*

Chem. A, 2019, **123**, 7920-7931.
85. Q. Meng and J. Chen, *J. Chem. Phys.*, 2019, **150**, 044307.
86. H. Wang, J. Fang, H. Yang, J. Song and Y. Li, *Chem. Phys. Lett.*, 2019, **730**, 227-233.
87. J. Espinosa-Garcia, M. Garcia-Chamorro, J. C. Corchado, S. Bhowmick and Y. V. Suleimanov, *Phys. Chem. Chem. Phys.*, 2020, **22**, 13790-13801.
88. J. Fang, W. Fan, H. Yang, J. Song and Y. Li, *Chin. J. Chem. Phys.*, in press, DOI: 10.1063/1674-0068/cjcp2007117.
89. C. Rangel, M. Garcia-Chamorro, J. C. Corchado and J. Espinosa-Garcia, *Phys. Chem. Chem. Phys.*, 2020, **22**, 14796-14810.
90. H. Yang, W. Fan, J. Fang, J. Song and Y. Li, *Chin. J. Chem. Phys.*, in press, DOI: 10.1063/1674-0068/cjcp2007121.
91. D. Chandler and P. G. Wolynes, *J. Chem. Phys.*, 1981, **74**, 4078-4095.
92. Y. V. Suleimanov, F. J. Aoiz and H. Guo, *J. Phys. Chem. A*, 2016, **120**, 8488-8502.
93. S. Habershon, D. E. Manolopoulos, T. E. Markland and T. F. Miller, 3rd, *Annu. Rev. Phys. Chem.*, 2013, **64**, 387-413.
94. J. O. Richardson and S. C. Althorpe, *J. Chem. Phys.*, 2009, **131**, 214106.
95. T. J. Hele and S. C. Althorpe, *J. Chem. Phys.*, 2013, **138**, 084108.
96. Bennett, C. H. Molecular Dynamics and Transition State Theory: The Simulation of Infrequent Events. In Algorithms for Chemical Computations; ACS Symposium Series; Christofferson, R. E., Ed.; American Chemical Society: Washington, DC, 1977; Vol. 46.
97. D. Chandler, *J. Chem. Phys.*, 1978, **68**, 2959-2970.
98. Y. V. Suleimanov, J. W. Allen and W. H. Green, *Comput. Phys. Commun.*, 2013, **184**, 833-840.
99. M. J. Gillan, *Phys. Rev. Lett.*, 1987, **58**, 563-566.
100. G. A. Voth, D. Chandler and W. H. Miller, *J. Chem. Phys.*, 1989, **91**, 7749-7760.
101. T. E. Markland and D. E. Manolopoulos, *J. Chem. Phys.*, 2008, **129**, 024105.
102. J. Kastner and W. Thiel, *J. Chem. Phys.*, 2005, **123**, 144104.
103. J. Kästner, *Wiley Interdiscip. Rev.: Comput. Mol. Sci.*, 2011, **1**, 932-942.
104. H. C. Andersen, *J. Chem. Phys.*, 1980, **72**, 2384-2393.
105. H. C. Andersen, *J. Comput. Phys.*, 1983, **52**, 24-34.
106. X. Hu, W. L. Hase and T. Pirraglia, *J. Comput. Chem.*, 1991, **12**, 1014-1024.
107. W. L. Hase, R. J. Duchovic, X. Hu, A. Komornicki, K. F. Lim, D. H. Lu, G. H. Peslherbe, K. N. Swamy, S. R. R. V. Linde and A. Varandas, *J. Quantum Chem. Program Exch. Bull.*, 1996, **16**, 671.
108. J. L. B. J. Zheng, R. Meana-Pañeda, S. Zhang, B. J. Lynch, J. C. Corchado, Y.-Y. Chuang, P. L. Fast, W.-P. Hu, Y.-P. Liu, G. C. Lynch, K. A. Nguyen, C. F. Jackels, A. Fernández Ramos, B. A. Ellingson, V. S. Melissas, J. Villà, I. Rossi, E. L. Coitiño, J. Pu, T. V. Albu, A. Ratkiewicz, R. Steckler, B. C. Garrett, A. D. Isaacson, and D. G. Truhlar, 2018.
109. B. C. Garrett and D. G. Truhlar, *J. Am. Chem. Soc.*, 1979, **101**, 4534-4548.
110. Y. P. Liu, D. H. Lu, A. Gonzalez-Lafont, D. G. Truhlar and B. C. Garrett, *J. Am. Chem. Soc.*, 1993, **115**, 7806-7817.
111. G. A. Natanson, B. C. Garrett, T. N. Truong, T. Joseph and D. G. Truhlar, *J. Chem. Phys.*, 1991, **94**, 7875-7892.
112. C. F. Jackels, Z. Gu and D. G. Truhlar, *J. Chem. Phys.*, 1995, **102**, 3188-3201.
113. Y. Y. Chuang and D. G. Truhlar, *J. Phys. Chem. A*, 1997, **101**, 3808-3814.
114. À. González-Lafont and J. M. Lluch, *Wiley Interdiscip. Rev.: Comput. Mol. Sci.*, 2016, **6**, 584-603.

Table 1 Input parameters for the RPMD calculations on the H + O_3 → OH + O_2 reaction.

Parameter	Values	Note
Command line parameters		
T	150, 220, 298, 360, 480, 640	Temperature (K)
n(H)	8 (480K, 640K); 16 (298K, 360K);	Number of beads
	32 (220K); 64 (150K)	
n(D)	4 (640K); 8 (480K);	
	16 (220K, 298K, 360K); 32 (150K)	
Dividing surface parameters		
R_∞	20	Dividing surface s_1 parameter (a_0)
N_{bonds}	1	Number of forming and breaking bonds
$N_{channel}$	2	Number of equivalent product channels
Thermostat		
thermostat	Andersen	Thermostat option
Biased sampling parameters		
$N_{windows}$	72	Number of windows
ξ_1	-0.03	Center of the first window
$d\xi$	0.03 (all for -0.03≤ξ≤0.66)	Window spacing step
	0.01 (all for 0.66＜ξ≤0.90)	
	0.005 (all for 0.90＜ξ≤1.02)	
ξ_N	1.02	Center of the last window
dt	0.0001	Time step (ps)
k_i	0.680 (all for -0.03＜ξ≤0.66)	Umbrella force constant ((T/K) eV)
	2.721 (all for 0.66＜ξ≤0.90)	
	13.605 (150K, 220K for 0.90＜ξ≤1.02)	
	10.884 (298K, 360K for 0.90＜ξ≤1.02)	
	8.163 (480K,640K for 0.90＜ξ≤1.02)	
Biased sampling parameters		
$N_{trajectory}$	60	Number of trajectories
$t_{equilibration}$	20	Equilibration period (ps)
$t_{sampling}$	100	Sampling period in each trajectory (ps)
N_i	6×10^7	Total number of sampling points
Potential of mean force calculation		
ξ_0	-0.03	Start of umbrella integration
$\xi^{\neq}$	1.02	End of umbrella integration
N_{bins}	5000	Number of bins
Recrossing factor calculation		

dt	0.0001	Time step (ps)
$t_{equilibration}$	20	Equilibration period (ps) in the constrained (parent) trajectory
$N_{totalchild}$	100000	Total number of unconstrained (child) trajectories
$t_{childsampling}$	2	Sampling increment along the parent trajectory (ps)
N_{child}	100	Number of child trajectories per one initially constrained configuration
t_{child}	0.1	Length of child trajectories (ps)

Table 2 Results from RPMD, CVT/μOMT and QCT calculations of the rate coefficients for the H + $O_3 \rightarrow$OH + O_2 reaction.

T / K	150	220	298	360	480	640
N_{beads}	64	32	16	16	8	8
$\xi^{\ddagger}$	0.941	0.982	0.995	0.999	1.002	1.006
$\Delta G(\xi^{\ddagger})$	0.058834	0.118821	0.156545	0.179316	0.223339	0.277297
k_{QTST}	6.66×10^{-11}	1.46×10^{-11}	2.00×10^{-11}	3.02×10^{-11}	5.10×10^{-11}	8.54×10^{-11}
κ	0.082470	0.640717	0.804929	0.804949	0.78428	0.780583
k_{RPMD}	5.49×10^{-12}	9.37×10^{-12}	1.61×10^{-11}	2.43×10^{-11}	4.00×10^{-11}	6.67×10^{-11}
k_{1BEAD}	9.36×10^{-13}	2.89×10^{-12}	8.31×10^{-12}	1.49×10^{-11}	3.09×10^{-11}	5.56×10^{-11}
$k_{\text{CVT/}\mu\text{OMT}}$	2.63×10^{-12}	6.06×10^{-12}	1.19×10^{-11}	1.78×10^{-11}	3.19×10^{-11}	5.59×10^{-11}
k_{QCT}	1.12×10^{-12}	4.33×10^{-12}	1.02×10^{-11}	1.68×10^{-11}	3.27×10^{-11}	5.97×10^{-11}

Table 3 Results from RPMD, CVT/μOMT and QCT calculations of the rate coefficients for the D + O_3 → OD + O_2 reaction.

T / K	150	220	298	360	480	640
N_{beads}	32	16	16	16	8	4
$\xi^{\ddagger}$	0.977	0.996	1.001	1.002	1.005	1.008
$\Delta G(\xi^{\ddagger})$	0.089973	0.130661	0.162357	0.184004	0.221621	0.276701
k_{QTST}	4.61×10^{-12}	4.41×10^{-12}	1.14×10^{-11}	1.86×10^{-11}	3.80×10^{-11}	6.48×10^{-11}
κ	0.445073	0.782174	0.797001	0.791958	0.773816	0.768201
k_{RPMD}	5.49×10^{-12}	9.37×10^{-12}	1.61×10^{-11}	1.47×10^{-11}	2.94×10^{-11}	4.98×10^{-11}
k_{1BEAD}	6.84×10^{-13}	2.11×10^{-12}	6.32×10^{-12}	1.09×10^{-11}	2.29×10^{-11}	4.02×10^{-11}
$k_{\text{CVT/}\mu\text{OMT}}$	1.13×10^{-12}	3.45×10^{-12}	7.67×10^{-12}	1.20×10^{-11}	2.28×10^{-11}	4.03×10^{-11}
k_{QCT}	7.73×10^{-13}	3.31×10^{-12}	7.79×10^{-11}	1.27×10^{-11}	2.41×10^{-11}	4.35×10^{-11}

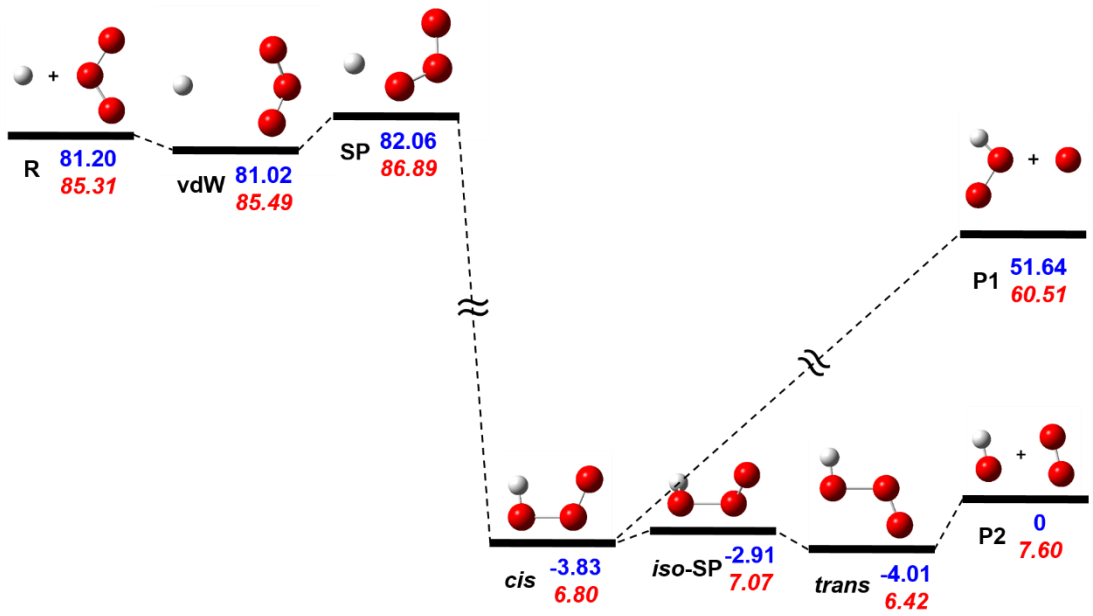

Fig. 1 Energetics of the H + O_3 → OH + O_2 and H + O_3 → HO_2 + O reactions on the $HO_3(X^2A'')$ PES. The energies are relative to the minimum of the OH + O_2 asymptote potential in kcal/mol. The values indicated by blue are energies of stationary points obtained from the PES and their corrections with ZPE are shown in red italic.

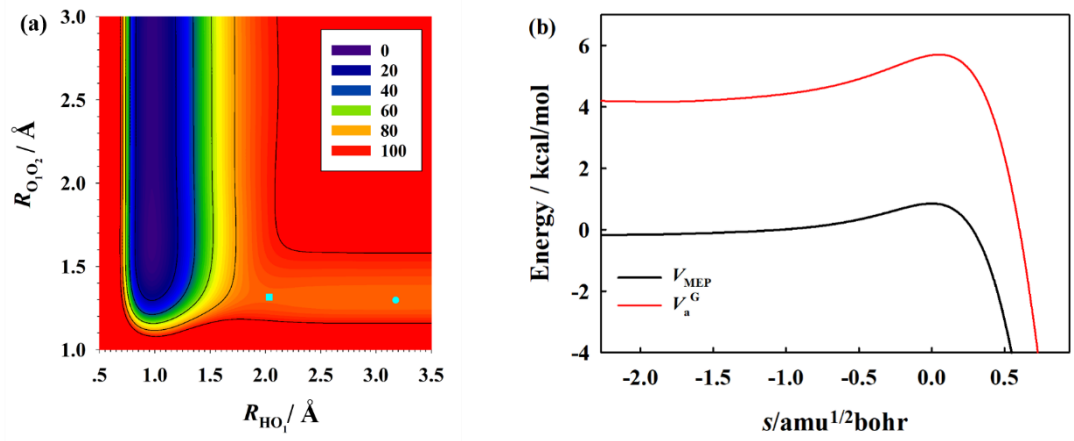

Fig. 2 (a) Contour plots of the PES for the H + O_3 → OH + O_2 reaction as a function of the distances between two bonded O atoms ($R_{O_1O_2}$) and between the H and a terminal (R_{HO_1}). The other four coordinates are optimized. Energies are in kcal/mol with respect to the trans-HO_3 complex; (b) the MEP and vibrationally adiabatic ground-state energy as a function of the mass-dependent IRC *s*.

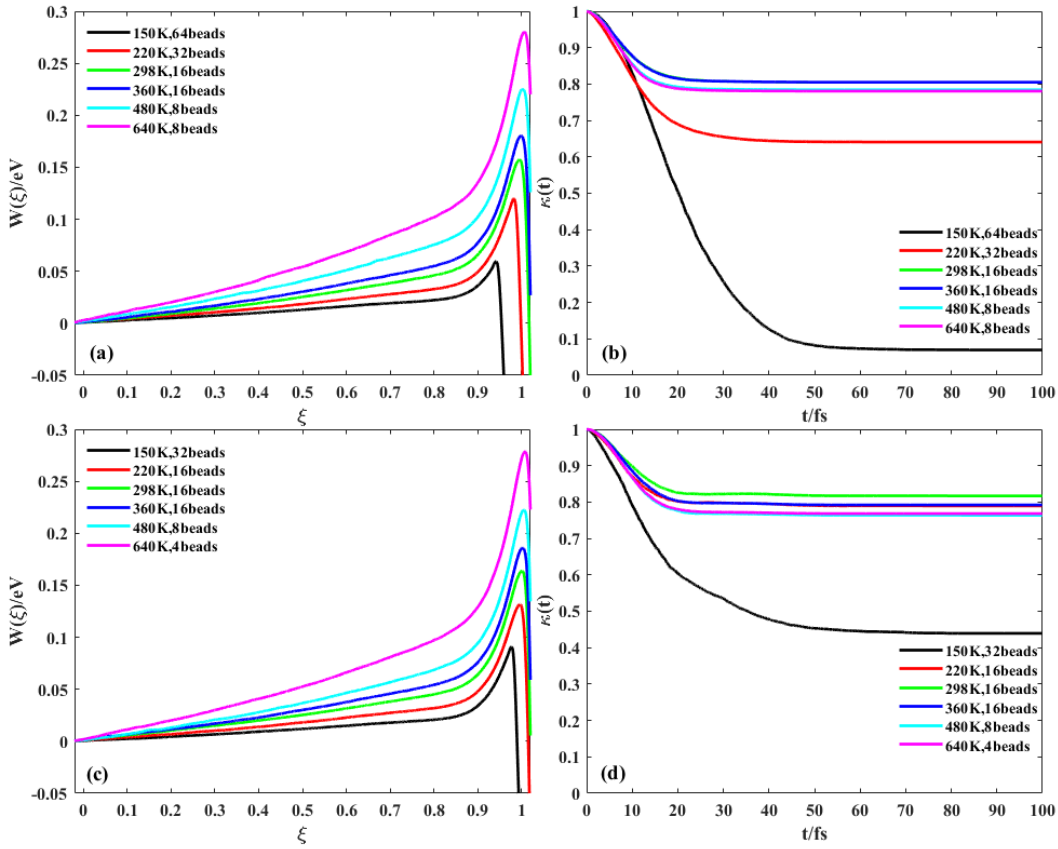

Fig. 3 Converged RPMD PMF curves and transmission coefficients for the H + O_3 reaction (a, b) and D + O_3 reaction (c, d) at 150, 220, 298, 360, 480, and 640 K.

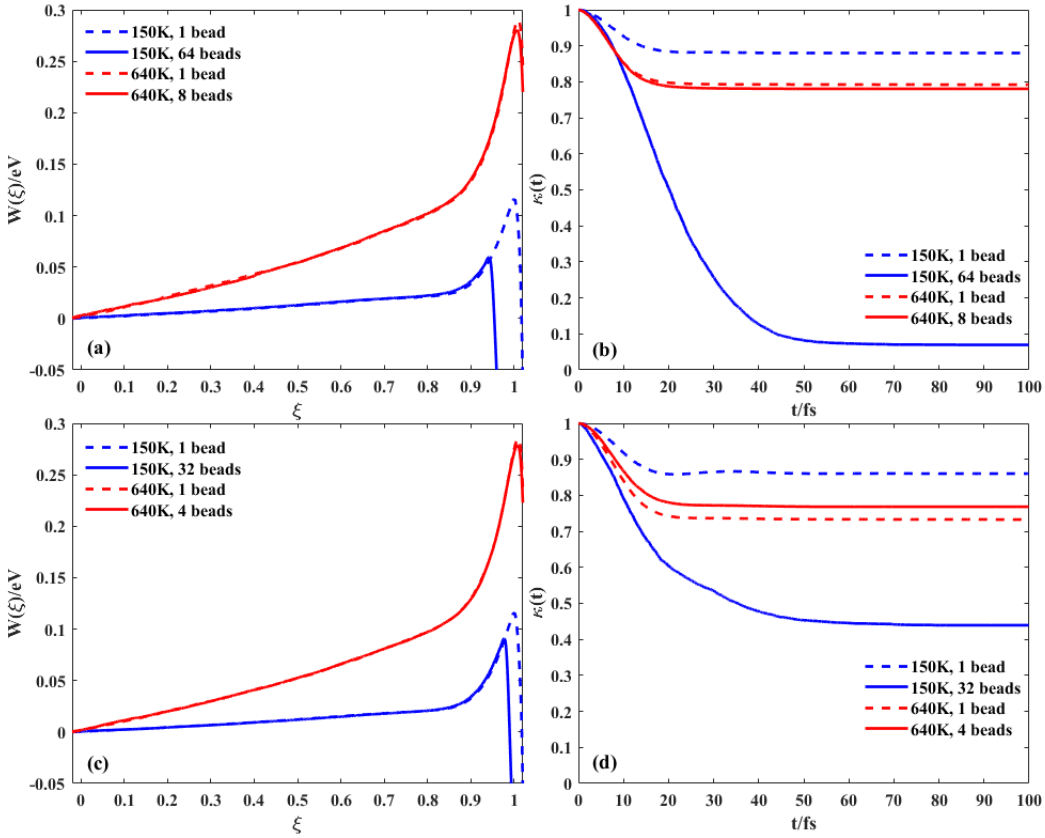

Fig. 4 RPMD PMF curves and transmission coefficients with one bead and the converged number of beads at 150 K and 640 K for the H + O_3 reaction (a, b) and D + O_3 reaction (c, d).

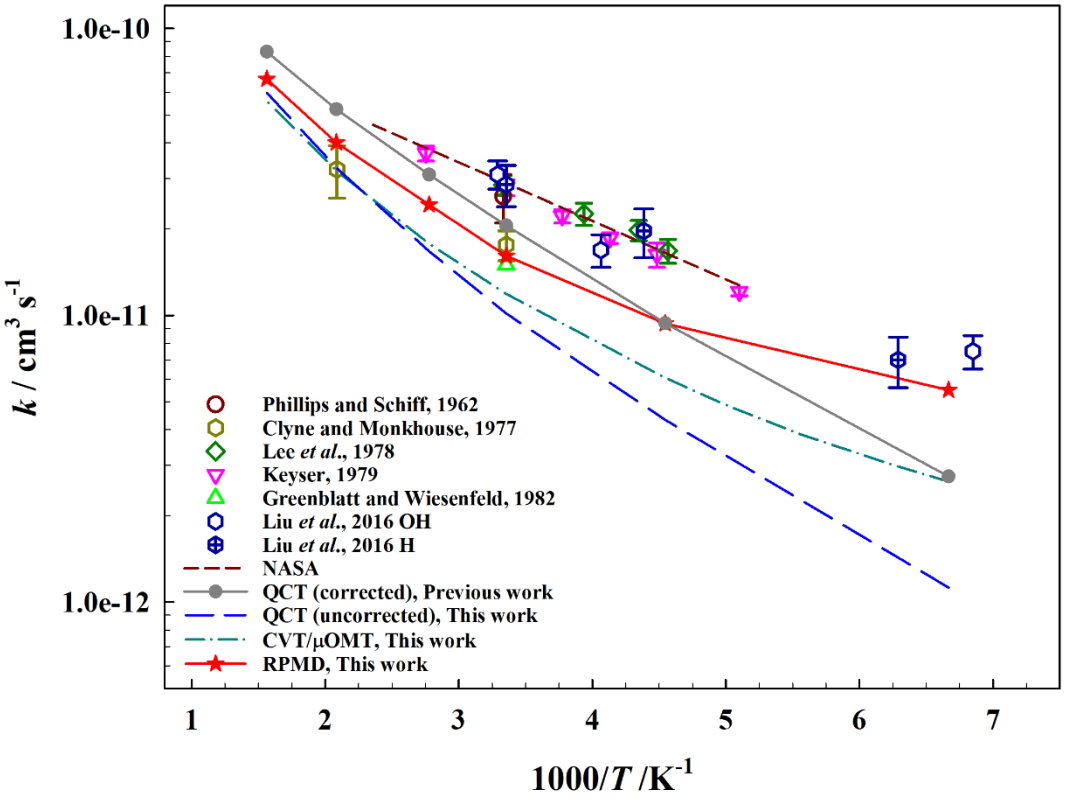

Fig. 5 Arrhenius plot for the H + O_3 → OH + O_2 reaction rate coefficients obtained with the RPMD and CVT/μOMT methods on the PIP-NN PES. For comparison, previous experimental results are also included.

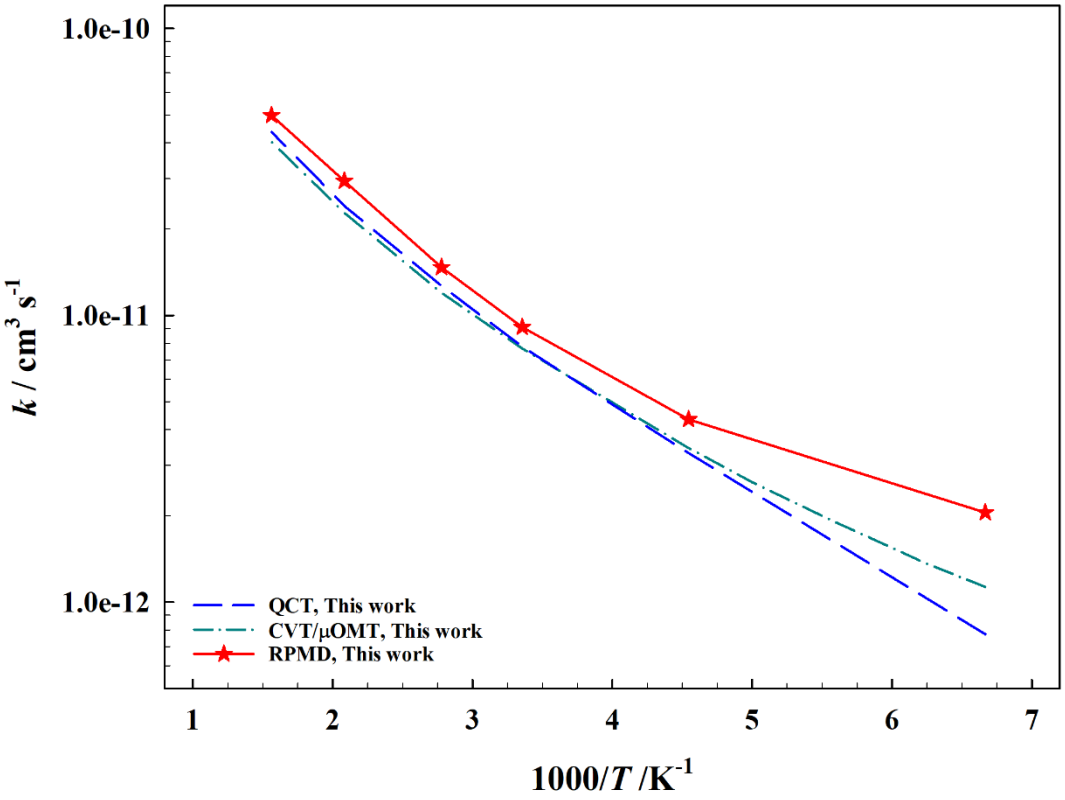

Fig. 6 Arrhenius plot for the D + O_3 → OD + O_2 reaction obtained with the RPMD, CVT/μOMT and QCT methods on the PIP-NN PES.

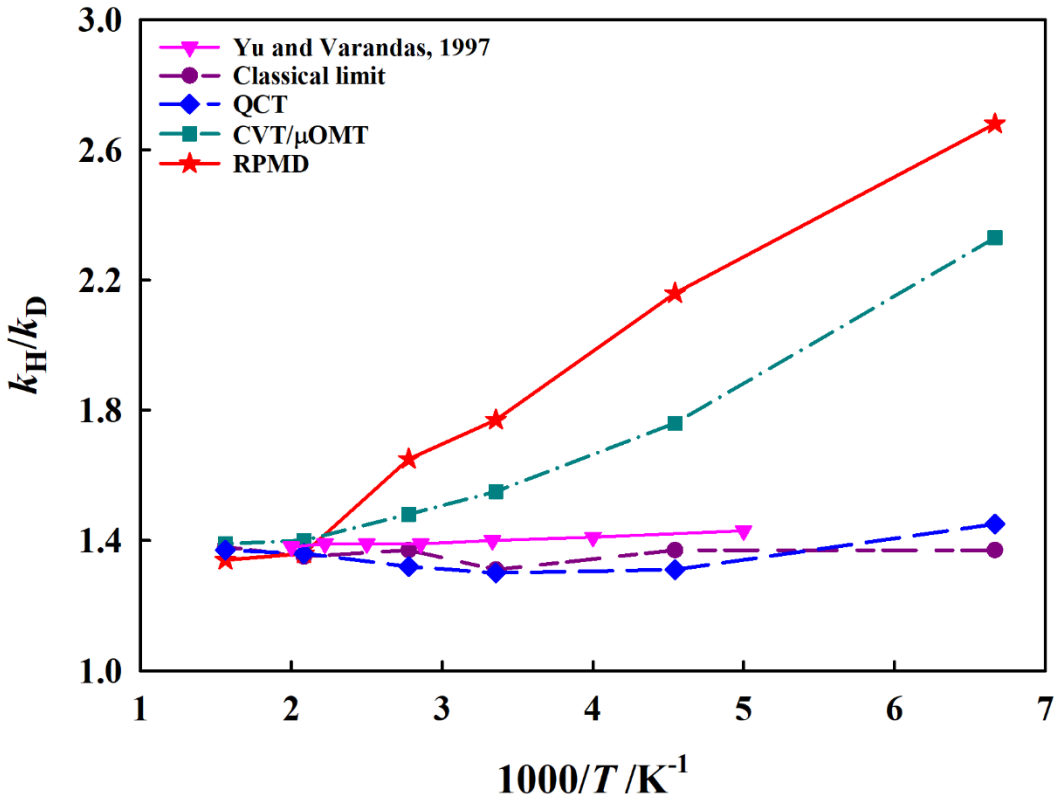

Fig. 7 Comparison of the calculated KIEs for the H/D + O_3⟶ OH/OD + O_2 reaction with different methods.

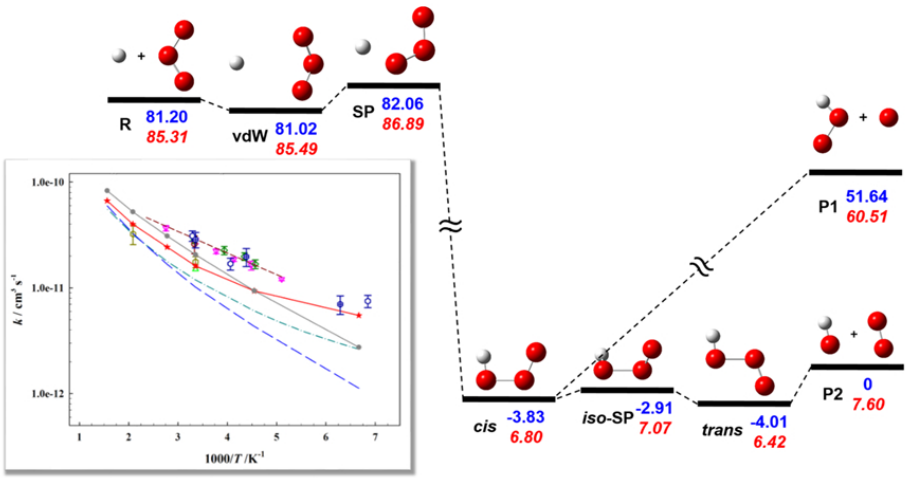

80x39mm (300 x 300 DPI)